NeRF−−: Neural Radiance Fields Without Known Camera Parameters

ZIRUI WANG, Active Vision Lab, University of Oxford
SHANGZHE WU, Visual Geometry Group, University of Oxford
WEIDI XIE, Visual Geometry Group, University of Oxford
MIN CHEN, e-Research Centre, University of Oxford
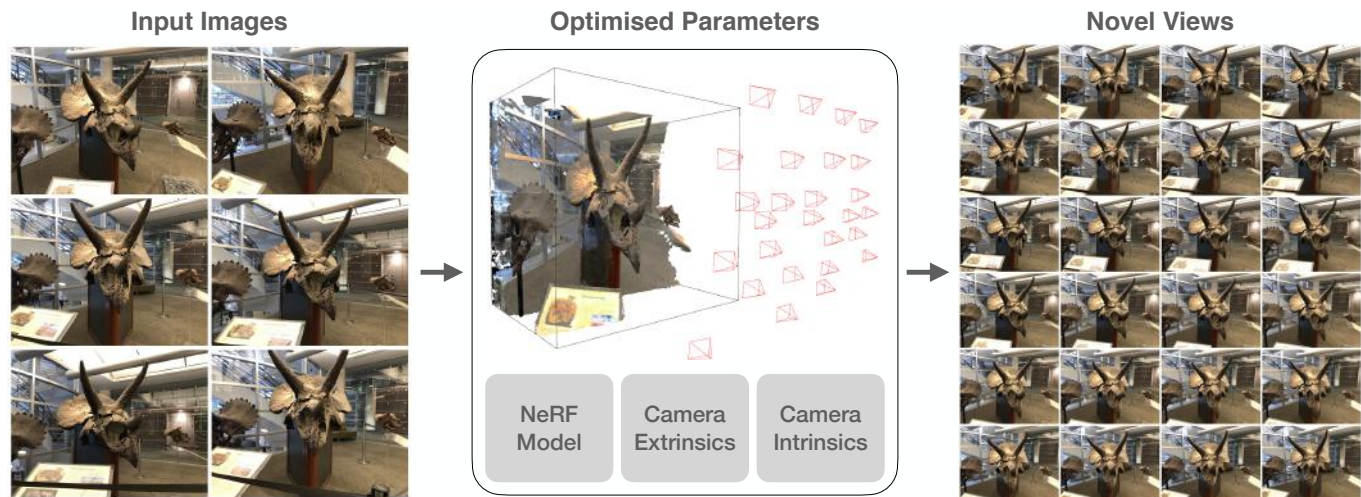VICTOR ADRIAN PRISACARIU, Active Vision Lab, University of Oxford

Figure 1. We propose *NeRF−−*, a NeRF-based framework for novel view synthesis without pose supervision. Specifically, given only a sparse set of uncalibrated images of a scene as input, with unknown camera parameters, our pipeline estimates the camera extrinsics and intrinsics of the input images, and simultaneously trains a Neural Radiance Field (NeRF) via joint optimisation. This allows us to render new images from novel, unseen viewpoints.

This paper tackles the problem of novel view synthesis (NVS) from 2D images without known camera poses or intrinsics. Among various NVS techniques, Neural Radiance Field (NeRF) has recently gained popularity due to its remarkable synthesis quality. Existing NeRF-based approaches assume that the camera parameters associated with each input image are either directly accessible at training, or can be accurately estimated with conventional techniques based on correspondences such as Structure-from-Motion. In this work, we propose an end-to-end framework, termed *NeRF−−*, for training NeRF models given only RGB images, without pre-computed camera parameters. Specifically, we show that the camera parameters, including both intrinsics and extrinsics, can be automatically discovered via joint optimisation during the training of the NeRF model. On the standard LLFF benchmark, our model achieves novel view synthesis results on par with the baseline trained with COLMAP pre-computed camera parameters. We also conduct extensive analyses to understand the model behaviour under different camera trajectories, and show that in scenarios where COLMAP fails, our model still produces robust results.

CCS Concepts: • **Computing methodologies** → **Rendering**; **Shape representations**; **Tracking**; **Reconstruction**.

Additional Key Words and Phrases: Neural radiance field representation (NeRF), novel view synthesis, camera pose estimation, deep learning.

Authors' addresses: Zirui Wang, Active Vision Lab, University of Oxford, ryan@robots.ox.ac.uk; Shangzhe Wu, Visual Geometry Group, University of Oxford, szwu@robots.ox.ac.uk; Weidi Xie, Visual Geometry Group, University of Oxford, weidi@robots.ox.ac.uk; Min Chen, e-Research Centre, University of Oxford, min.chen@oerc.ox.ac.uk; Victor Adrian Prisacariu, Active Vision Lab, University of Oxford, victor@robots.ox.ac.uk.

1 INTRODUCTION

The ability to fly through our three-dimensional world has been the dream of human beings for thousands of years — from the 3500-year-old story of Daedalus and Icarus in ancient Greek mythology, to the earliest scientific attempts of Leonardo da Vinci to build flying machines in the late 1400s [Niccoli 2006]. Thanks to the recent advances in virtual reality (VR) technology, it is now possible to capture a digital version of our world and generate arbitrary views, allowing us to traverse the world through a virtual lens.

To generate photo-realistic views of a real-world scene from any viewpoint, it not only requires to understand the 3D scene geometry, but also to model complex viewpoint-dependent appearance resulting from sophisticated light transport phenomena. One way to achieve this is by constructing a so-called 5D plenoptic function that directly models the light passing through each point in space [Adelson and Bergen 1991] (or a 4D light field [Gortler et al. 1996; Levoy and Hanrahan 1996] if we restrict ourselves outside the convex hull of the objects of interest). Unfortunately, it is not feasible in practice to physically measure a densely sampled plenoptic function. As an alternative, Novel View Synthesis (NVS) aims to approximate such a dense light field from only sparse observations, such as a small set of images captured from diverse viewpoints.

In literature, a large amount of research effort has been devoted to developing methods for novel view synthesis. One group aims to

explicitly reconstruct the surface geometry and the appearance on the surface from the observed sparse views [Chaurasia et al. 2013; Debevec et al. 1996; Hedman et al. 2017; Waechter et al. 2014; Wiles et al. 2020; Zitnick et al. 2004]. For the purpose of reconstructing 3D geometry from 2D images, techniques like Structure-from-Motion (SfM) [Faugeras and Luong 2001] establish correspondences and simultaneously estimate the camera parameters if they are not directly available. However, these methods often struggle to synthesise high-fidelity images due to imperfect surface reconstruction and limited capacity for modelling complex view-dependent effects, such as specularity, transparency and global illumination.

Another group of approaches adopt volume-based representations to directly model the appearance of the entire space [Mildenhall et al. 2019, 2020; Penner and Zhang 2017; Sitzmann et al. 2019; Zhou et al. 2018], and use volumetric rendering techniques to generate images. This enables smooth gradients for photometry-based optimisation, and is capable of modelling highly complex shapes and materials with sophisticated view-dependent effects. Among these approaches, Neural Radiance Fields (NeRF) have recently gained popularity due to its exceptional simplicity and performance for synthesising high-quality images of complex real-world scenes. The key idea in NeRF is to represent the entire volume space with a continuous function, parameterised by a multi-layer perceptron (MLP), bypassing the need to discretise the space into voxel grids, which usually suffers from resolution constraints.

In both groups of research, camera calibration is often assumed to be prerequisite, while in practise, this information is rarely accessible, and requires to be pre-computed with conventional techniques, such as SfM. In particular, NeRF [Mildenhall et al. 2020] and its variants [Martin-Brualla et al. 2020; Park et al. 2020; Zhang et al. 2020] use COLMAP [Schonberger and Frahm 2016] to estimate the camera parameters (both intrinsics and extrinsics) associated with each input image. This pre-processing step, apart from introducing additional complexity, also suffers from dynamic scenes [Kopf et al. 2020; Park et al. 2020] or the presence of significant view-dependent appearance changes, as a result, making the NeRF training dependent on the robustness and accuracy of the camera parameter estimation.

In this paper, we ask the question: do we really need to pre-compute camera parameters when training a view synthesis model such as a NeRF? We show that the answer is no. The NeRF model is in fact able to automatically discover the camera parameters by itself during training. Specifically, we propose *NeRF−−*, which jointly optimises the 3D scene representation and the camera parameters (both extrinsics and intrinsics). On the standard LLFF benchmark, we demonstrate comparable novel view synthesis results to the *baseline NeRF* trained with COLMAP pre-computed camera parameters. Additionally, we also analyse the model behaviour under different camera trajectories, showing that in scenarios where COLMAP fails, our model still produces robust results, which suggests that the joint optimisation can lead to more robust reconstruction, echoing the Bundle Adjustment (BA) in classical SfM pipelines [Triggs et al. 2000].

2 RELATED WORK

There is vast literature on novel views synthesis. It can be roughly divided into two categories, one with explicit surface modelling, and the other with dense volume-based representations.

The first group of approaches aim to explicitly reconstruct the surface geometry and model its appearance for novel view rendering. To reconstruct the 3D geometry from 2D images, traditional techniques, such as SfM [Faugeras and Luong 2001; Hartley and Zisserman 2003] and Simultaneous Localisation and Mapping (SLAM) jointly solve for the 3D geometry and the associated camera parameters, by establishing feature correspondences (*e.g.* MonoSLAM[Davison et al. 2007], ORB-SLAM [Mur-Artal et al. 2015], Bundler [Snavely et al. 2006], COLMAP [Schonberger and Frahm 2016]), or photometric errors, e.g. DTAM [Newcombe et al. 2011] and LSD-SLAM [Engel et al. 2014]. However, many of these methods assume diffuse surface texture, and do not recover view-dependent appearance, hence resulting in unrealistic novel view rendering. Multi-view photometric stereo methods [Zhou et al. 2013], on the other hand, aim to explain view-dependent appearance with sophisticated hand-crafted material BRDF models, but suffer from the trade-off between quality and complexity. Recent works such as [Riegler and Koltun 2020a,b] integrates meshes and features from images to handle such view-dependent appearance synthesis. Ultimately, even though explicit geometry reconstruction facilitates camera parameter estimation, modelling photo-realistic appearance for novel views is still a challenging task.

As an alternative, volume-based representations have been proposed to directly model the appearance of the 3D space [Flynn et al. 2016; Mildenhall et al. 2019, 2020; Penner and Zhang 2017; Seitz and Dyer 1999; Sitzmann et al. 2019; Zhou et al. 2018]. In recent years, researchers have proposed various volume-based representations of this kind, such as Soft3D [Penner and Zhang 2017], Multi-Plane Images (MPI) [Choi et al. 2019; Flynn et al. 2019; Mildenhall et al. 2019; Tucker and Snavely 2020; Zhou et al. 2018], Scene Representation Networks (SRN) [Sitzmann et al. 2019], Occupancy Networks [Mescheder et al. 2019; Yariv et al. 2020] and Neural Radiance Fields (NeRF) [Mildenhall et al. 2020]. These dense volumetric representations enable smooth gradients for photometry-based optimisation and has shown to be promising for photo-realistic novel view synthesis of highly complex shapes and appearance.

One common assumption in both groups of research is that, camera parameters for all input images are accessible, or can be accurately estimated by traditional SfM or SLAM techniques, such as COLMAP [Schonberger and Frahm 2016], Bundler [Snavely et al. 2006] and ORB-SLAM [Mur-Artal et al. 2015]. This usually refers to a two-stage system, where the view synthesis would be dependent on accurate camera parameter estimation. In this work, we propose an end-to-end framework, jointly optimising the camera parameters and a NeRF representation given only RGB images, while maintaining the capability to produce comparable view synthesis results.

In particular, a concurrent work, iNeRF [Yen-Chen et al. 2020], is closely related to ours. It shows that given a well-trained NeRF model, the 6DOF camera poses for novel views can be estimated by simply minimising the photometric rendering error. However,
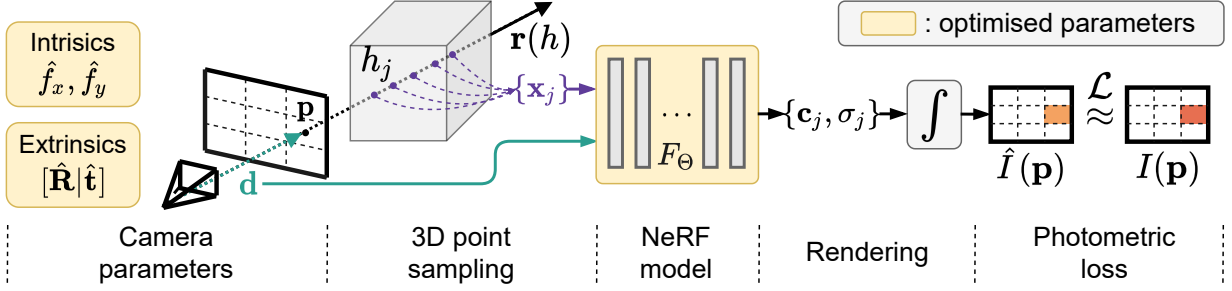
Figure 2. Our pipeline jointly optimises a NeRF model and the camera parameters of the input images by minimising the photometric reconstruction errors. To render a pixel p from NeRF, given the optimised camera parameters $(\hat{f}_x, \hat{f}_y, \hat{R}, \hat{t})$, we feed a number of 3D points x_j sampled along the camera ray together with the viewing direction d into NeRF F_Θ, and aggregate the output radiance c_j and densities σ_j to obtain its colour $\hat{I}(p)$. The entire pipeline is trained end-to-end using only RGB images with unknown cameras as input.

they assume a well-trained NeRF model to begin with, whereas our method is able to automatically discover the camera parameters from only RGB images in a fully unsupervised fashion.

Apart from novel views synthesis using multiple images, there are also learning-based approaches [Niklaus et al. 2019; Shih et al. 2020; Tucker and Snavely 2020; Wiles et al. 2020; Wu et al. 2020; Zhou et al. 2016], which allow for single-image novel view synthesis at inference time by learning a prior over a collection of training data. These methods, however, are either restricted to small camera motions, or produce low quality images, due to the limited information in a single input image.

3 PRELIMINARY

Given a set of images $\mathcal{I} = \{I_1, I_2, \ldots, I_N\}$ captured from N sparse viewpoints of a scene, with their associated camera parameters $\Pi = \{\pi_1, \pi_2, \ldots, \pi_N\}$, including both intrinsics and extrinsics, the goal of novel view synthesis is to come up with a scene representation that enables the generation of realistic images from novel, unseen viewpoints. In this paper, we follow the approach proposed in Neural Radiance Fields (NeRF) [Mildenhall et al. 2020].

In NeRF, the authors adopt a continuous function for constructing a volumetric representation of the scene from sparse input views. In essence, it models the view-dependent appearance of the 3D space using a continuous function $F_\Theta : (x, d) \rightarrow (c, \sigma)$, parameterised by a multi-layer perceptron (MLP). The function maps a location $x = (x, y, z)$ in 3D space together with a viewing direction $d = (\theta, \phi)$ to a radiance colour $c = (r, g, b)$ and a density value σ.

To render an image from a NeRF model, the colour at each pixel $p = (u, v)$ on the image plane ($\hat{I}_i$) is obtained by a rendering function $\mathcal{R}$, aggregating the radiance along a ray shooting from the camera position o_i, passing through the pixel p into the volume [Gortler et al. 1996; Max 1995]:

$$\hat{I}_i(p) = \mathcal{R}(p, \pi_i|\Theta) = \int_{h_n}^{h_f} T(h)\sigma(r(h)) c(r(h), d) \, dh, \quad (1)$$

where

$$T(h) = \exp\left(-\int_{h_n}^{h} \sigma(r(s)) \, ds\right) \quad (2)$$

denotes the accumulated transmittance along the ray, *i.e.*, the probability of the ray travelling from h_n to h without hitting any other particle, and $r(h) = o + hd$ denotes the camera ray that starts from camera origin o and passes through p, controlled by the camera parameter π_i, with near and far bounds h_n and h_f. In practice, the integral in Eq. (1) is approximated by accumulating radiance and densities of a set of sampled points along a ray.

With this implicit scene representation $F_\Theta(x, d)$ and a differentiable renderer $\mathcal{R}$, NeRF can be trained by minimising the photometric error between the observed views and synthesised ones under known camera parameters:

$$\mathcal{L} = \sum_{i}^{N} ||I_i - \hat{I}_i||_2^2 \quad (3)$$

$$\Theta^* = \arg\min_{\Theta} \mathcal{L}(\hat{I}|\mathcal{I}, \Pi), \quad (4)$$

where $\hat{I}$ denotes the set of synthesised images $\{\hat{I}_1, ..., \hat{I}_N\}$.

To summarise, NeRF represents a 3D scene as a radiance field parameterised by an MLP, which is trained with a set of sparsely observed images via a photometric reconstruction loss. Note that, the camera parameters π_i for these images are required for training, which are usually estimated by SfM packages, such as COLMAP [Schonberger and Frahm 2016]. For more details of NeRF, we refer the readers to [Mildenhall et al. 2020].

4 METHOD

In this paper, we show that the pre-processing step on estimating camera parameters π_i of the input images is in fact unnecessary. Unlike the training setup of the original NeRF, here, we only assume a set of RGB images $\mathcal{I}$ as inputs, without known camera parameters. We seek to jointly optimise the camera parameters and scene representation during the training. Mathematically, this can be written as:

$$\Theta^*, \Pi^* = \arg\min_{\Theta, \Pi} \mathcal{L}(\hat{I}, \hat{\Pi}|\mathcal{I}), \quad (5)$$

where the camera parameters Π include both the camera intrinsics and the camera extrinsics. Apart from simplifying the original two-stage approach, another motivation for such a joint optimisation approach comes from bundle adjustment in classical SfM

pipelines [Triggs et al. 2000] and SLAM systems [Davison et al. 2007; Engel et al. 2014; Newcombe et al. 2011], which is key step to obtain globally consistent reconstruction results.

In the following sections, we first introduce the representations for the camera parameters and then describe the process of the joint optimisation.

4.1 Camera Parameters

Camera Intrinsics. Assuming a pinhole camera model, the camera intrinsic parameters can be expressed by a matrix:

$$K = \begin{pmatrix} f_x & 0 & c_x \\ 0 & f_y & c_y \\ 0 & 0 & 1 \end{pmatrix}, \tag{6}$$

where f_x and f_y denote camera focal lengths along the width and the height of the sensor respectively, and c_x and c_y denote principle points in the image plane.

We assume that the camera principle points are located at sensor centre, *i.e.* $c_x \approx W/2$ and $c_y \approx H/2$, where H and W denote the height and the width of the image, and all input images are taken by the same camera. As a result, camera intrinsics estimation reduces to estimating two values, the focal lengths f_x and f_y, which can be directly optimised as trainable parameters during training.

Camera Extrinsics. The camera extrinsic parameters determine the position and orientation of the camera, expressed as a transformation matrix $T_{wc} = [R|t]$ in SE(3), where $R \in$ SO(3) denotes the camera rotation and $t \in \mathbb{R}^3$ denotes the translation. Since translation vector t is defined in Euclidean space, it can be directly optimised as trainable parameters during training.

As for the camera rotation, which is defined on SO(3), we adopt the axis-angle representation: $\phi := \alpha\omega, \phi \in \mathbb{R}^3$, where a rotation is represented by a normalised rotation axis ω and a rotation angle α. This can be converted to a rotation matrix R using the Rodrigues' formula:

$$R = I + \frac{\sin(\alpha)}{\alpha}\phi^\wedge + \frac{1 - \cos(\alpha)}{\alpha^2}(\phi^\wedge)^2, \tag{7}$$

where the skew operator $(\cdot)^\wedge$ converts a vector ϕ to a skew matrix:

$$\phi^\wedge = \begin{pmatrix} \phi_0 \\ \phi_1 \\ \phi_2 \end{pmatrix}^\wedge = \begin{pmatrix} 0 & -\phi_2 & \phi_1 \\ \phi_2 & 0 & -\phi_0 \\ -\phi_1 & \phi_0 & 0 \end{pmatrix}. \tag{8}$$

With this parameterisation, we can optimise the camera extrinsics for each input image I_i with the trainable parameters ϕ_i and t_i during training.

To summarise, the set of camera parameters that we directly optimise in our model are the camera intrinsics f_x and f_y shared by all input images, and the camera extrinsics parameterised by ϕ_i and t_i specific to each image I_i.

4.2 Joint Optimisation of NeRF and Camera Parameters

Our goal is to train a NeRF model given only RGB images as input, without known camera parameters. In other words, we need to find out the camera parameters associated with each input image while training the NeRF model.

Recall that NeRF is trained by minimising the photometric reconstruction error on the input views. Specifically, for each training

image I_i, we randomly select M pixel locations $\{p_{i,m}\}_{m=1}^M$, which we would like to reconstruct from the NeRF model F_Θ. To render the colour of each pixel $p_{i,m} = (u, v)$, we shoot a ray $\hat{r}_{i,m}(h)$ from the camera position through the pixel into the radiance field, with the current estimates of the camera parameters $\hat{\pi}_i = (\hat{f}_x, \hat{f}_y, \hat{\phi}_i, \hat{t}_i)$:

$$\hat{r}_{i,m}(h) = \hat{o}_i + h\hat{d}_{i,m}, \tag{9}$$

where

$$\hat{d}_{i,m} = \hat{R}_i \begin{pmatrix} (u - W/2)/\hat{f}_x \\ -(v - H/2)/\hat{f}_y \\ -1 \end{pmatrix}, \tag{10}$$

$\hat{o}_i = \hat{t}_i$ and $\hat{R}_i$ is computed from $\hat{\phi}_i$ using Eq. (7).

We then sample a number of 3D points $\{x_j\}$ along the ray and evaluate the radiance colours $\{c_j\}$ and the density values $\{\sigma_j\}$ at these locations via the NeRF network F_Θ. The rendering function Eq. (1) is then applied to obtain the colour of that pixel $\hat{I}_{i,m}$ by aggregating the predicted radiance and densities along the ray.

For each reconstructed pixel, we compute photometric loss using Eq. (3) by comparing its predicted colour $\hat{I}_{i,m}$ against the ground-truth colour $I_{i,m}$ sampled from the input image. Since the entire pipeline is fully differentiable, we can jointly optimise both the parameters of the NeRF model Θ and the camera parameters $\{\pi_i\}$ by minimising the reconstruction loss. The pipeline is summarised in Algorithm 1.

For initialisation, the cameras for all input images are located at origin looking towards $-z$-axis, *i.e.* all $\hat{R}_i$ are initialised with identity matrices and all t_i with zero vectors, and the focal lengths f_x and f_y are initialised to be the width W and the height H respectively, *i.e.* FOV $\approx 53°$.

Refinement. Although the above joint optimisation of both the camera parameters and the NeRF model from scratch produces reasonable results, the model could fall into local minima where the optimised camera parameters are sub-optimal, resulting in slightly blurry synthesised images. Thus, we introduce an optional refinement step to further improve the quality of the synthesised images. Specifically, after the first training process is completed, we drop the trained NeRF model and re-initialise it with random parameters while keeping the pre-trained camera parameters. We then repeat the joint optimisation using the pre-trained camera parameters as initialisation. We find this additional refinement step generally leads to sharper images and improves the synthesis results, as evidenced by the comparison in Table 1.

Additionally, the camera parameters can also be initialised with estimated values from external toolboxes, where they are available, and jointly refined during the training of the NeRF model. We conduct experiments to refine the camera parameters estimated using COLMAP during NeRF training, and find the novel view results slightly improved through the joint refinement, as shown in Table 1.

5 EXPERIMENTS

We conduct experiments on diverse scenes and compare with the original *baseline NeRF*, where camera parameters of input images are estimated with COLMAP. In the following sections, we describe the experiment setup, followed by various results and analyses. We
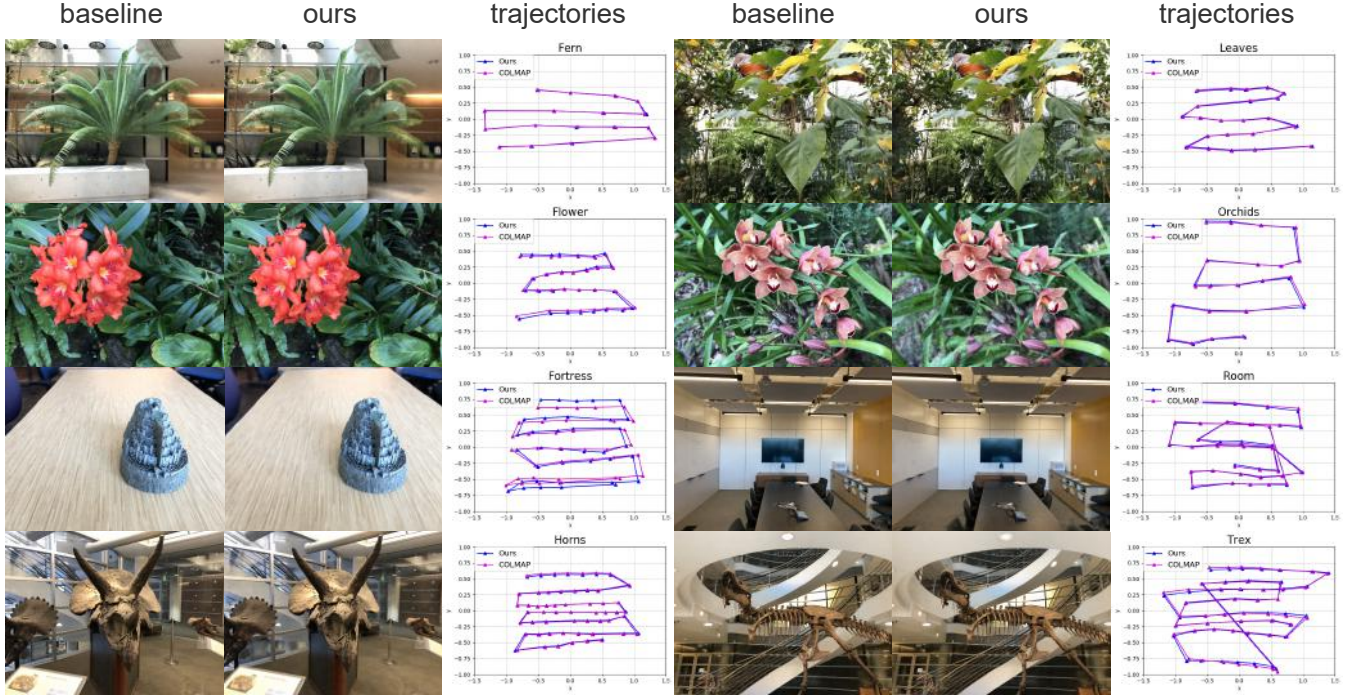
Figure 3. Qualitative comparison between our *NeRF−−* model with unknown cameras and the *baseline NeRF* on LLFF-NeRF dataset. For each example, on the left, we show the synthesised novel views from the *baseline NeRF* with COLMAP pre-computed camera parameters and from our model with jointly optimised camera parameters; on the right, we compare our optimised camera trajectories with the ones estimated from COLMAP, aligned using ATE. Our proposed *NeRF−−* model recovers accurate camera poses and produces high quality novel views comparable to the *baseline NeRF*.

ALGORITHM 1: *NeRF−−* Pipeline

Input: N images $\mathcal{I} = \{I\}_{i=1}^{N}$

Output: NeRF model F_Θ, camera parameters $[\hat{\boldsymbol{\phi}}_i]$, $[\hat{\boldsymbol{t}}_i]$, $\hat{f}_x$ and $\hat{f}_y$

import torch.nn as nn

// Initialisation
$[\hat{\boldsymbol{\phi}}_i]$ = nn.Parameter(shape=(N, 3), require_grad=True)
$[\hat{\boldsymbol{t}}_i]$ = nn.Parameter(shape=(N, 3), require_grad=True)
$\hat{f}_x, \hat{f}_y$ = nn.Parameter(shape=(2,), require_grad=True)
// NeRF structure see our supp.
F_Θ = NeRF_Module(require_grad=True)
// Training
for i *in* range *(N)* **do**
    for m *in* range *(M)* **do**
        $\hat{\boldsymbol{d}}_{i,m}$ = construct_ray($\hat{\boldsymbol{\phi}}_i, \hat{\boldsymbol{t}}_i, \hat{f}_x, \hat{f}_y, \boldsymbol{p}_{i,m}$) // Eq. 10
        for h *from* h_n *to* h_f **do**
            $\boldsymbol{x}_j$ = sample_point($\hat{\boldsymbol{d}}_{i,m}, \hat{\boldsymbol{t}}_i, h$) // Eq. 5
            $\boldsymbol{c}_h, \sigma_j = F_\Theta(\boldsymbol{x}_h, \hat{\boldsymbol{d}}_{i,m})$ // forward NeRF
        end
        $\hat{I}_{i,m}$ = render_ray($[\boldsymbol{c}_h], [\sigma_h]$)
    end
    L = loss($\hat{I}_i, I_i$) // Eq. 5
    L.backward()
    optimiser.update($[\hat{\boldsymbol{\phi}}_i], [\hat{\boldsymbol{t}}_i], \hat{f}_x, \hat{f}_y, \hat{\Theta}$)
end

---

also include a discussion on the limitations of the current method at the end of the section.

5.1 Setup

5.1.1 Dataset. We first conduct experiments on the same forward-facing dataset as that in NeRF, namely, LLFF-NeRF [Mildenhall et al. 2019], which has 8 forward-facing scenes captured by mobile phones or consumer cameras, each containing 20-62 images. In all experiments, we follow the official pre-processing procedures and train/test splits, *i.e.* the resolution of the training images is 756×1008, and every 8-th image is used as the test image.

To understand the behaviour of NVS under different camera motion scenarios, such as rotation, traversal (horizontal motion) and zoom-in, we additionally collected a number of diverse scenes extracted from the short video segments in RealEstate10K [Zhou et al. 2018] and Tanks&Temples [Knapitsch et al. 2017] dataset, as well as a few more clips captured by ourselves. In particular, we only select the video sequences with the desired motion type from corresponding datasets. The image resolution in these sequences varies between 480×640 and 1080×1920 and the frame rate ranges from 24 fps to 60 fps. We sub-sample the frames and reduce the frame rates to 3-6 fps, and each sequence contains 7-40 images.

5.1.2 Metrics. We evaluate the proposed framework from two aspects: *First*, to measure the quality of novel view rendering, we use the common metrics: Peak Signal-to-Noise Ratio (PSNR), Structural

Scene	PSNR↑				SSIM↑				LPIPS↓			
	colmap	ours	colmap+r	ours+r	colmap	ours	colmap+r	ours+r	colmap	ours	colmap+r	ours+r
Fern	22.24	21.83	22.31	22.14	0.64	0.62	0.65	0.64	0.47	0.49	0.47	0.47
Flower	25.25	25.34	25.67	25.51	0.71	0.71	0.72	0.72	0.36	0.37	0.36	0.36
Fortress	27.68	26.55	27.53	27.44	0.72	0.67	0.70	0.71	0.38	0.44	0.41	0.39
Horns	24.35	23.13	24.51	23.65	0.68	0.63	0.68	0.66	0.44	0.49	0.44	0.46
Leaves	18.82	18.73	19.00	18.88	0.52	0.52	0.53	0.53	0.47	0.47	0.46	0.47
Orchids	18.92	16.50	19.23	16.86	0.51	0.38	0.52	0.40	0.46	0.56	0.45	0.54
Room	27.83	25.73	27.89	26.21	0.87	0.83	0.87	0.84	0.40	0.44	0.40	0.42
Trex	23.21	22.49	23.36	22.97	0.75	0.72	0.75	0.74	0.41	0.44	0.41	0.42
Mean	23.54	22.54	23.69	22.96	0.68	0.64	0.68	0.66	0.42	0.46	0.43	0.44

Table 1. Quantitative comparison between our model and the *baseline NeRF* on LLFF-NeRF dataset, with optional refinement (+r). The results show that: (1) The NVS quality of our method with unknown cameras is comparable to the *baseline NeRF* (colmap vs. ours: ΔPSNR = 1.0, ΔSSIM and ΔLPIPS < 0.05), (2) Additional joint refinement of the camera parameters with a re-initialised NeRF model leads to slightly more optimal results on both our model and the *baseline NeRF* (colmap+r/ours+r vs. colmap/ours).

Similarity Index Measure (SSIM) [Wang et al. 2004] and Learned Perceptual Image Patch Similarity (LPIPS) [Zhang et al. 2018]; *Second*, apart from perceptual quality, we also evaluate the accuracy of the optimised camera parameters. However, as ground truth are not accessible for real scenes, we can only evaluate the accuracy by computing the difference between our optimised camera and the estimations obtained from COLMAP. For focal length evaluation, we report the absolute error in the metric of pixels. For the camera poses, we follow the evaluation protocol of the Absolute Trajectory Error (ATE) [Sturm et al. 2012; Zhang and Scaramuzza 2018], which first aligns two sets of pose trajectories globally using a similarity transformation Sim(3) and reports the rotation angle between two rotations and the absolute distance between two translation vectors.

5.1.3 Implementation Details. We implement our framework in PyTorch following the same architecture as original *baseline NeRF*, except that, for computation efficiency, we: (a) *do not* use the hierarchical sampling strategy; (b) reduce the hidden layer dimension from 256 to 128; and (c) sample only 128 points along each ray. We use Kaiming initialisation [He et al. 2015] for the NeRF model, and initialise all cameras to be at origin looking at $-z$ direction, with focal lengths f_x and f_y to be the width and the height of the image. We use three separate Adam optimisers for NeRF, camera poses and focal lengths respectively, all with an initial learning rate of 0.001, except that we lower the initial NeRF learning rate to 0.0005 for *Fortress* scene. The learning rate of the NeRF model is decayed every 10 epochs by multiplying with 0.9954 (exponential decay), and learning rates of the pose and focal length parameters are decayed every 100 epochs with a multiplier of 0.9. For each training epoch, we randomly sample 1024 pixels from every input image and 128 points in NeRF along each ray to synthesise the colour of the pixels. All models are trained for 10000 epochs unless otherwise specified. More technical details are included in the supplementary material. We will release the code.

5.2 Results

In this section, we present the experimental results and in-depth analyses on the proposed framework, *i.e. NeRF−−*. In Section 5.2.1, we demonstrate the results for novel view synthesis in terms of

Figure 4. Qualitative comparison of NVS quality between our model and *baseline NeRF* on RealEstate10K dataset. Our model produces better results on the first two examples but slightly worse results on the last two examples, indicating comparable performance overall compared to *baseline NeRF*.

perceptual qualities. In Section 5.2.2, we show the evaluation of the optimised camera parameters. Lastly, in Section 5.2.3, to understand the model behaviour under different camera motion patterns, we demonstrate some qualitative results and discussion for sequences under controlled camera motions, *e.g.* rotational, traversal, and zoom-in. More results and visualisations are provided in the supplementary material.

5.2.1 On Novel View Synthesis Quality. In this section, we compare the perceptual qualities from the novel views rendered by *baseline NeRF* (where camera parameters are estimated from COLMAP), and our proposed model *NeRF−−*, which jointly optimises the camera parameters and the 3D scene representation from only RGB images.

Since our optimised camera parameters might lie in different spaces from the ones estimated using COLMAP, for evaluation, we first align the two trajectories globally with a Sim(3) transformation using an ATE toolbox [Zhang and Scaramuzza 2018], followed by a more fine-grained gradient-driven camera pose alignment by minimising the photometric error on the synthesised image, while keeping the NeRF model *fixed*. Finally, we compute the metrics between the test image and our synthesised image rendered from the best possible viewpoint. Simply put, all the above mentioned processing aims to eliminate the effect from camera mis-alignment and make a fair comparison on quality of the 3D scene representation.

We report the quantitative evaluations in Table 1 and visual results in Figure 3. Overall, our joint optimisation model, which does not require camera parameters as inputs, achieves similar NVS quality compared to the *baseline NeRF* model. This confirms that jointly optimising the camera parameters and 3D scene representation is indeed possible. Nevertheless, we observe that for both the *Orchids* and the *Room*, our *NeRF−−* model produces slightly worse results compared to the *baseline NeRF*. We also notice from Table 2 that the difference between optimised camera focal lengths and COLMAP estimation are most noticable for these two scenes (196.50 and 343.6). This suggests that the optimisation might have fallen into local minima with sub-optimal intrinsics. More discussion can be found in Section 5.3.

In Table 1, we also show the results with additional refinement step, which has shown to improve the NVS quality for both the *baseline NeRF* and our proposed *NeRF−−* model slightly.

5.2.2 On Camera Parameter Estimation.
We evaluate the accuracy of the camera parameter estimation on the LLFF-NeRF dataset. As explained in Section 5.1.2, the ground-truth camera parameters for these sequences are not available, we therefore treat the COLMAP estimation as references, and report the difference betwen our optimised camera parameters and theirs on the training images.

In Table 2, we show the L1 difference on the estimated focal lengths, and metrics on camera rotation and translation computed with the ATE toolbox [Zhang and Scaramuzza 2018], which accounts for global scale ambiguity. In the first set of columns (Focal + Pose + NeRF), the camera poses obtained from our model are close to those estimated from COLMAP, confirming the effectiveness of the joint optimisation pipeline. This can also be visualised by the aligned camera trajectories on xy-plane in Figure 3. The error on camera intrinsics is however much larger. This is due to the notorious ambiguity between camera intrinsics and the scale of the camera translation [Pollefeys and Van Gool 1997], especially for these forward facing scenes.

We conduct another two sets of experiments: 1) We fix the camera poses to be same as from COLMAP, and only optimise the camera focal lengths jointly with the NeRF model. We then measure the difference between the optimised focal lengths and the COLMAP estimated ones. As indicated by the second set of columns (Focal + NeRF) in Table 2, by fixing the camera extrinsics, the focal length has been recovered. 2) We fix the focal lengths to be same as from COLMAP estimation, and only the camera extrinsics are jointly optimised with the NeRF model. The results are reported in the
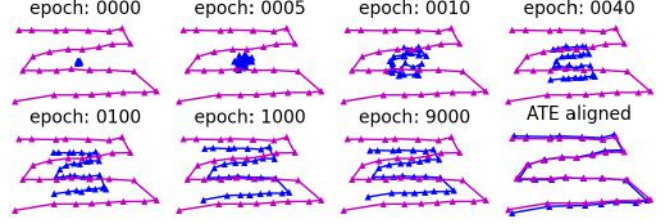

Figure 5. History of camera pose optimisation during training, visualised on xy-plane (purple: COLMAP, blue: ours). Starting from identity, our optimised camera poses gradually converge towards COLMAP estimations after about 1000 epochs, subject to a similarity transformation.

same table *Pose+NeRF*, showing similar performance as the joint optimisation.

Visualisation of the optimisation process. For a better understanding of the optimisation process, we provide a visualisation of the camera poses at various training epochs for the scene *Flower* from the LLFF-NeRF dataset (Figure 5). The pose estimations are initialised to be identity matrices at the beginning, and converged after about 1000 epochs, subject to a similarity transformation between optimised camera parameters and those estimated from COLMAP.

5.2.3 On Different Camera Motion Patterns.
To inspect how our system performs under different camera motions, we pick a number of sequences from the additional datasets (RealEstate10K, Tanks & Temples), with the camera motions following the desired patterns, such as rotation, traversal (horizontal motion) and zoom-in. To give an overview of the experimental results, both the *baseline NeRF* and our joint training approach work well for zoom-in camera motions, whereas in rotational and traversal movements, we find that the COLMAP sometimes produces incorrect camera poses or simply fails to converge. We provide more discussions for each motion pattern in the following sections.

Rotational Motion. Despite being one common camera motion in hand-held video capturings, rotational motion is notoriously difficult to model in SfM or SLAM systems, as no 3D points can be triangulated under such a motion [Pirchheim et al. 2013; Svoboda et al. 1998; Szeliski and Shum 1997]. In the literature, numerous approaches have been proposed to deal with this problem, for example, through rotation averaging [Bustos et al. 2019; Hartley et al. 2013].

In Figure 6, we show the NVS results of a sequence from the RealEstate10K dataset, where the camera motion is dominated by a rotation. In this case, COLMAP produces incorrect camera poses with extreme outliers, leading to a failure for training *baseline NeRF*. After manually correcting two extreme outlier poses by assigning to their closest ones, we then re-train the NeRF model, shown as the last row in Figure 6. Even with such manually corrected poses, the *baseline NeRF* still produces blurry synthesis results and fails to model the geometry correctly. In comparison, our joint optimisation model recovers much more accurate geometry and consequently higher quality view synthesis results.

Apart from picking video sequence from the public datasets, we also show results on the sequence recorded by ourselves (Figure 7),

Scene	(E1) Focal + Pose + NeRF				(E2) Focal + NeRF		(E3) Pose + NeRF		
	Focal↓	Rotation (deg)↓	Translation↓	PSNR↑	Focal↓	PSNR↑	Rotation (deg)↓	Translation↓	PSNR↑
Fern	138.10	1.199	0.007	21.83	3.77	21.75	6.484	0.012	20.80
Flower	36.58	3.836	0.011	25.34	1.75	24.44	4.287	0.005	24.91
Fortress	105.40	1.899	0.041	26.55	0.61	27.40	2.933	0.024	25.14
Horns	130.80	3.299	0.015	23.13	2.16	24.02	3.595	0.015	23.08
Leaves	91.03	7.202	0.006	18.73	4.49	18.42	1.667	0.003	18.44
Orchids	196.50	4.727	0.018	16.50	1.36	18.57	8.289	0.025	16.44
Room	343.60	3.142	0.013	25.73	2.94	27.34	3.279	0.048	25.32
Trex	89.00	6.042	0.013	22.49	2.99	22.80	6.577	0.020	22.15
Mean	141.38	3.92	0.02	22.54	2.509	23.09	4.639	0.019	22.04

Table 2. Quantitative evaluation of our optimised focal lengths and camera poses on LLFF-NeRF dataset. We report the difference between our optimised camera parameters and COLMAP computed ones for the lack of ground-truth on real scenes. The results show that: (1) our optimised camera poses are very close to COLMAP estimations (E1 - Rot. & Trans.); (2) our model converges to a different solution for camera intrinsics as it is highly ambiguous (E1 - Foc.); (3) with the same camera poses, our model is able to recover similar focal lengths (E2 - Foc.); (4) similarly, with the same focal lengths, our model still recovers similar camera poses (E3 - Rot. & Trans.). See more discussions in Section 5.2.2.
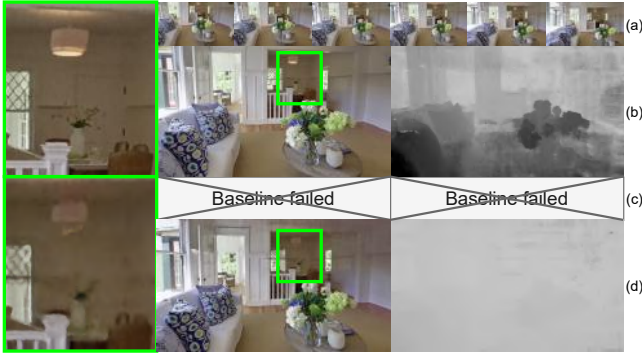

Figure 6. Camera motion analysis - rotation-dominant. We compare our results with *baseline NeRF* on a rotation-dominant sequence. Row (a) shows thumbnails of our training images. Row (b) shows novel view and depth renderings of our method. Row (c) illustrates that the *baseline NeRF* fails on this scene due to incorrect camera pose estimations from COLMAP. Row (d) shows the results of the *baseline NeRF* with COLMAP poses where outliers are manually corrected. On the left, we show a zoomed-in region of both (a) and (d). Our method recovers accurate geometry and produces high quality novel views, whereas the *baseline NeRF* fails with COLMAP poses and still produces poor results even with manually corrected poses.

Figure 7. Camera motion analysis - pure rotation. Top: input images. Bottom: optimised camera poses, rendered novel view and rendered depth map. Our model is able to render high-quality novel views, even though the depth map is incorrect, which is expected since no geometry information is captured in a rotation sequence.

where the camera motion is almost purely rotational. This is akin to shooting a panorama image, where the frames can simply be stitched together by homography transformations [Pirchheim et al. 2013; Svoboda et al. 1998; Szeliski and Shum 1997]. In this case, COLMAP fails to estimate the camera parameters, and thus, no results can be produced by the *baseline NeRF*. Our joint optimisation pipeline, in contrast, still produces reasonable camera estimation and novel view synthesis results. Note that the geometry in this case is poorly reconstructed, as shown in the rendered depth map, since no disparity information is available with such purely rotational camera motions.

Traversal Motion. Traversal Motion refers to the motion pattern where the camera moves along a horizontal trajectory. We show two examples from Tanks&Temples, and RealEstate10K in Figures 8 and 9, where the camera roughly follows a traversal pattern. Our approach produces reasonable camera parameter estimations and synthesis results on both sequences, whereas COLMAP fails on the second scene due to close to critical plane [Luong and Faugeras 1994; Torr et al. 1998].

Zoom-in Motion. In Figure 10, we show an example captured with a zooming-in camera, both COLMAP and our system recover reasonable camera trajectories and view synthesis results.

5.3 Limitations and Future Work

Although the proposed framework for jointly optimising camera parameters and 3D scene representation demonstrates promising results, we still observe a few limitations.

Firstly, as with other photometry-based reconstruction methods, it often struggles to reconstruct scenes with large texture-less regions or in the presence significant photometric inconsistency across frames, such as motion blur, changes in brightness or colour. For example, the joint optimisation struggles to converge on the *Fortress* scene from the LLFF-NeRF dataset (although it works well with a lower learning rate on the NeRF model). This is likely to
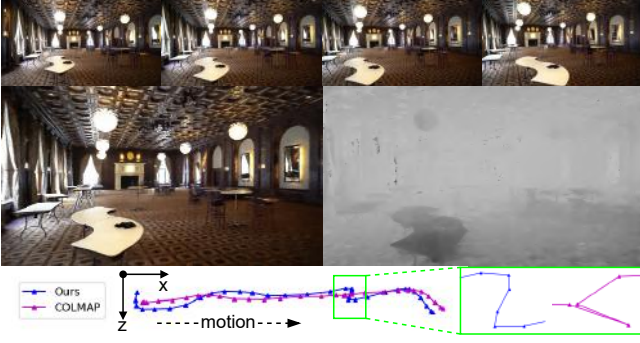
Figure 8. Camera motion analysis - roughly traversal. Top: input images. Middle: our rendered novel view and rendered depth. Bottom: visualisation of our optimised camera trajectory and COLMAP estimated trajectory. Both our model and the *baseline NeRF* model produce high-quality results, although COLMAP seems to produce unlikely camera trajectory illustrated in the zoomed-in segment.
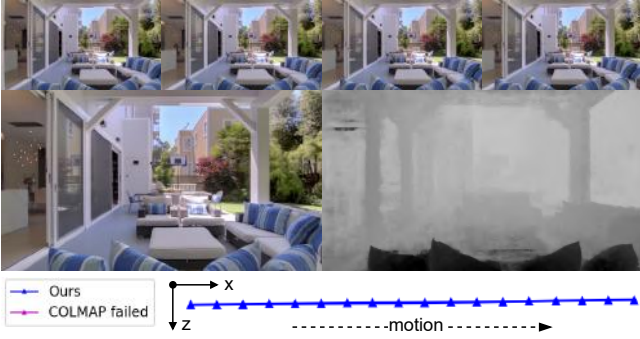

Figure 9. Camera motion analysis - traversal. Top: input images. Middle: our rendered novel view and rendered depth. Bottom: visualisation of our optimised camera trajectory. While our model produces high-quality results with accurate geometry, COLMAP fails to estimate the camera poses from the input images, hence no results from *baseline NeRF*.

Figure 10. Camera motion analysis - zoom-in. Left: visualisation of our optimised camera trajectory. Right: input images, our rendered novel view and rendered depth. Our approach produces similar pose estimations compared to COLMAP

be caused by large areas of repeated textures, which could potentially be mitigated by incorporating feature-level losses or explicitly attending to distinctive feature points during training.

Secondly, jointly optimizing camera parameters and scene reconstruction is notoriously challenging and could potentially fall into local minima. For instance, as discussed in Section 5.2.1, our joint optimisation pipeline produces inferior synthesis results on *Orchids* and *Room* compared to *baseline NeRF* shown in Table 1, largely due to sub-optimal optimisation results for the camera intrinsics (as indicated by the significant difference between our optimised focal lengths and the ones from COLMAP reported in Table 2). Incorporating additional components for explicit geometric matching might be useful in guiding the optimisation process.

Lastly, the proposed framework is limited to roughly forward-facing scenes and relatively short camera trajectories, since the NeRF model still struggles to model real scenes in $360°$ or large camera displacements [Zhang et al. 2020]. As for future work, exploiting the temporal information in sequences can be an effective regularisation for longer trajectories.

6 CONCLUSIONS

In this work, we present an end-to-end NeRF-based pipeline, called *NeRF−−*, for novel view synthesis from sparse input views, which does not require any information about the camera parameters for training. Specifically, our model jointly optimise the camera parameters for each input image while simultaneously training the NeRF model. This eliminates the need of pre-computing the camera parameters using potentially erroneous SfM methods (*e.g.* COLMAP) and still achieves comparable view synthesis results as the COLMAP-based NeRF baseline. We present extensive experimental results and demonstrate the effectiveness of this joint optimisation framework under different camera trajectory patterns, even when the baseline COLMAP fails to estimate the camera parameters. Despite its current limitations discussed above, our proposed joint optimisation pipeline has demonstrated promising results on this highly challenging task, which presents a step forward towards novel view synthesis on more general scenes with an end-to-end approach.

ACKNOWLEDGEMENT

REFERENCES

Edward H. Adelson and James R. Bergen. 1991. The Plenoptic Function and the Elements of Early Vision. In *Computational Models of Visual Processing*.

Álvaro Parra Bustos, Tat-Jun Chin, Anders Eriksson, and Ian Reid. 2019. Visual slam: Why bundle adjust?. In *ICRA*.

Gaurav Chaurasia, Sylvain Duchêne, Olga Sorkine-Hornung, and George Drettakis. 2013. Depth Synthesis and Local Warps for Plausible Image-based Navigation. In *SIGGRAPH*.

Inchang Choi, Orazio Gallo, Alejandro Troccoli, Min H Kim, and Jan Kautz. 2019. Extreme view synthesis. In *CVPR*.

Andrew J Davison, Ian D Reid, Nicholas D Molton, and Olivier Stasse. 2007. MonoSLAM: Real-time single camera SLAM. *TPAMI* (2007).

Paul E. Debevec, Camillo J. Taylor, and Jitendra Malik. 1996. Modeling and Rendering Architecture from Photographs: A Hybrid Geometry- and Image-Based Approach. In *SIGGRAPH*.

Jakob Engel, Thomas Schöps, and Daniel Cremers. 2014. LSD-SLAM: Large-scale direct monocular SLAM. In *ECCV*.

Olivier Faugeras and Quang-Tuan Luong. 2001. *The Geometry of Multiple Images*.

John Flynn, Michael Broxton, Paul Debevec, Matthew DuVall, Graham Fyffe, Ryan Overbeck, Noah Snavely, and Richard Tucker. 2019. Deepview: View synthesis with learned gradient descent. In *CVPR*.

John Flynn, Ivan Neulander, James Philbin, and Noah Snavely. 2016. Deep Stereo: Learning to Predict New Views from the World's Imagery. In *CVPR*.

Steven J. Gortler, Radek Grzeszczuk, Richard Szeliski, and Michael F. Cohen. 1996. The Lumigraph. In *SIGGRAPH*.

Richard Hartley, Jochen Trumpf, Yuchao Dai, and Hongdong Li. 2013. Rotation averaging. *IJCV* (2013).

Richard Hartley and Andrew Zisserman. 2003. *Multiple view geometry in computer vision*.

Kaiming He, Xiangyu Zhang, Shaoqing Ren, and Jian Sun. 2015. Delving deep into rectifiers: Surpassing human-level performance on imagenet classification. In *ICCV*.

Peter Hedman, Suhib Alsisan, Richard Szeliski, and Johannes Kopf. 2017. Casual 3D Photography. In *SIGGRAPH Asia*.

Arno Knapitsch, Jaesik Park, Qian-Yi Zhou, and Vladlen Koltun. 2017. Tanks and Temples: Benchmarking Large-Scale Scene Reconstruction. *ToG* (2017).

Johannes Kopf, Xuejian Rong, and Jia-Bin Huang. 2020. Robust Consistent Video Depth Estimation. *arXiv preprint arXiv:2012.05901* (2020).

Marc Levoy and Pat Hanrahan. 1996. Light Field Rendering. In *SIGGRAPH*.

Q-T Luong and Olivier D Faugeras. 1994. A stability analysis of the fundamental matrix. In *ECCV*.

Ricardo Martin-Brualla, Noha Radwan, Mehdi S. M. Sajjadi, Jonathan T. Barron, Alexey Dosovitskiy, and Daniel Duckworth. 2020. NeRF in the Wild: Neural Radiance Fields for Unconstrained Photo Collections. *arXiv preprint arXiv:2008.02268* (2020).

Nelson Max. 1995. Optical models for direct volume rendering. *IEEE Transactions on Visualization and Computer Graphics* (1995).

Lars Mescheder, Michael Oechsle, Michael Niemeyer, Sebastian Nowozin, and Andreas Geiger. 2019. Occupancy Networks: Learning 3D Reconstruction in Function Space. In *CVPR*.

Ben Mildenhall, Pratul P. Srinivasan, Rodrigo Ortiz-Cayon, Nima Khademi Kalantari, Ravi Ramamoorthi, Ren Ng, and Abhishek Kar. 2019. Local Light Field Fusion: Practical View Synthesis with Prescriptive Sampling Guidelines. In *CVPR* (2019).

Ben Mildenhall, Pratul P Srinivasan, Matthew Tancik, Jonathan T Barron, Ravi Ramamoorthi, and Ren Ng. 2020. NeRF: Representing scenes as neural radiance fields for view synthesis. In *ECCV*.

Raul Mur-Artal, Jose Maria Martinez Montiel, and Juan D Tardos. 2015. ORB-SLAM: a versatile and accurate monocular SLAM system. *TRO* (2015).

Richard A Newcombe, Steven J Lovegrove, and Andrew J Davison. 2011. DTAM: Dense tracking and mapping in real-time. In *ICCV*.

Riccardo Niccoli. 2006. *History of Flight: From the Flying Machine of Leonardo Da Vinci to the Conquest of the Space*. White Star.

Simon Niklaus, Long Mai, Jimei Yang, and Feng Liu. 2019. 3D Ken Burns Effect from a Single Image. *ToG* (2019).

Keunhong Park, Utkarsh Sinha, Jonathan T. Barron, Sofien Bouaziz, Dan B Goldman, Steven M. Seitz, and Ricardo Martin-Brualla. 2020. Deformable Neural Radiance Fields. *arXiv preprint arXiv:2011.12948* (2020).

Eric Penner and Li Zhang. 2017. Soft 3D Reconstruction for View Synthesis. In *SIGGRAPH Asia*.

Christian Pirchheim, Dieter Schmalstieg, and Gerhard Reitmayr. 2013. Handling pure camera rotation in keyframe-based SLAM. In *International Symposium on Mixed and Augmented Reality (ISMAR)*.

Marc Pollefeys and Luc Van Gool. 1997. A stratified approach to metric self-calibration. In *CVPR*.

Gernot Riegler and Vladlen Koltun. 2020a. Free view synthesis. In *ECCV*.

Gernot Riegler and Vladlen Koltun. 2020b. Stable View Synthesis. *arXiv preprint arXiv:2011.07233* (2020).

Johannes L Schonberger and Jan-Michael Frahm. 2016. Structure-from-motion revisited. In *CVPR*.

Steven M. Seitz and Charles R. Dyer. 1999. Photorealistic Scene Reconstruction by Voxel Coloring. *IJCV* (1999).

Meng-Li Shih, Shih-Yang Su, Johannes Kopf, and Jia-Bin Huang. 2020. 3D Photography using Context-aware Layered Depth Inpainting. In *CVPR*.

Vincent Sitzmann, Michael Zollhöfer, and Gordon Wetzstein. 2019. Scene Representation Networks: Continuous 3D-Structure-Aware Neural Scene Representations. In *NeurIPS*.

Noah Snavely, Steven M Seitz, and Richard Szeliski. 2006. Photo tourism: exploring photo collections in 3D. In *SIGGRAPH*.

Jürgen Sturm, Nikolas Engelhard, Felix Endres, Wolfram Burgard, and Daniel Cremers. 2012. A benchmark for the evaluation of RGB-D SLAM systems. In *IROS*.

Tomáš Svoboda, Tomáš Pajdla, and Václav Hlaváč. 1998. Epipolar geometry for panoramic cameras. In *ECCV*.

Richard Szeliski and Heung-Yeung Shum. 1997. Creating full view panoramic image mosaics and environment maps. In *Computer Graphics and Interactive Techniques*.

Philip HS Torr, Andrew Zisserman, and Stephen J Maybank. 1998. Robust detection of degenerate configurations while estimating the fundamental matrix. *Computer Vision and Image Understanding* (1998).

Bill Triggs, Philip F. McLauchlan, Richard I. Hartley, and Andrew W. Fitzgibbon. 2000. Bundle Adjustment — A Modern Synthesis. In *Vision Algorithms: Theory and Practice*.

Richard Tucker and Noah Snavely. 2020. Single-view view synthesis with multiplane images. In *CVPR*.

Michael Waechter, Nils Moehrle, and Michael Goesele. 2014. Let There Be Color! — Large-Scale Texturing of 3D Reconstructions. In *ECCV*.

Zhou Wang, Alan C Bovik, Hamid R Sheikh, and Eero P Simoncelli. 2004. Image quality assessment: from error visibility to structural similarity. *IEEE Transactions on Image Processing* (2004).

Olivia Wiles, Georgia Gkioxari, Richard Szeliski, and Justin Johnson. 2020. SynSin: End-to-end View Synthesis from a Single Image. In *CVPR*.

Shangzhe Wu, Christian Rupprecht, and Andrea Vedaldi. 2020. Unsupervised learning of probably symmetric deformable 3d objects from images in the wild. In *CVPR*.

Lior Yariv, Yoni Kasten, Dror Moran, Meirav Galun, Matan Atzmon, Basri Ronen, and Yaron Lipman. 2020. Multiview Neural Surface Reconstruction by Disentangling Geometry and Appearance. In *NeurIPS*.

Lin Yen-Chen, Pete Florence, Jonathan T. Barron, Alberto Rodriguez, Phillip Isola, and Tsung-Yi Lin. 2020. iNeRF: Inverting Neural Radiance Fields for Pose Estimation. *arXiv preprint arXiv:2012.05877* (2020).

Kai Zhang, Gernot Riegler, Noah Snavely, and Vladlen Koltun. 2020. NeRF++: Analyzing and Improving Neural Radiance Fields. *arXiv preprint arXiv:2010.07492* (2020).

Richard Zhang, Phillip Isola, Alexei A Efros, Eli Shechtman, and Oliver Wang. 2018. The Unreasonable Effectiveness of Deep Features as a Perceptual Metric. In *CVPR*.

Zichao Zhang and Davide Scaramuzza. 2018. A Tutorial on Quantitative Trajectory Evaluation for Visual(-Inertial) Odometry. In *IROS*.

Tinghui Zhou, Richard Tucker, John Flynn, Graham Fyffe, and Noah Snavely. 2018. Stereo Magnification: Learning View Synthesis using Multiplane Images. In *SIGGRAPH*.

Tinghui Zhou, Shubham Tulsiani, Weilun Sun, Jitendra Malik, and Alexei A Efros. 2016. View Synthesis by Appearance Flow. In *ECCV*.

Zhenglong Zhou, Zhe Wu, and Ping Tan. 2013. Multi-view Photometric Stereo with Spatially Varying Isotropic Materials. In *CVPR*.

C. Lawrence Zitnick, Sing Bing Kang, Matthew Uyttendaele, Simon Winder, and Richard Szeliski. 2004. High-Quality Video View Interpolation Using a Layered Representation. In *SIGGRAPH*.

SUPPLEMENTARY MATERIAL

NeRF Architecture

We employ a smaller NeRF [Mildenhall et al. 2020] network than the original NeRF paper proposed without a hierarchical structure. Specifically, our NeRF implementation shrinks all hidden layer dimensions by half and follows the same positional encoding and skip connections as implemented in the original NeRF. The network architecture is presented in Fig. 11.
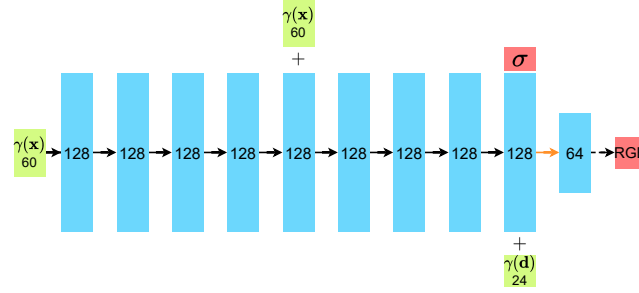

Figure 11. The NeRF implementation used in our paper. Green: position-encoded input. Blue: MLP hidden layers, with channel dimension shown inside. Red: radiance and density outputs. + denotes feature concatenation. Solid black arrow denotes layers with ReLU activation. Dashed black arrow denotes layers with Sigmoid activation. Orange arrow denotes layers without activation. We shrink all hidden layer dimensions in the original implementation by half, i.e. from 256 to 128 for the first 9 layers, and from 128 to 64 for the last layer. We employ the same number of positional encoding frequencies and the same skip links as in original NeRF. The figure style is borrowed from the original NeRF paper so readers can easily make comparisons.

Intrinsic Implementation Details

As mentioned in Sec. 4.2, we initialise our focal length f_x and f_y to be image size W and H. We parameterise this implementation by introducing two scale factors s_x and s_y:

$$f_x = s_x W \tag{11}$$
$$f_y = s_y H, \tag{12}$$

and initialise with $s_x = 1.0$ and $s_y = 1.0$. This parameterisation avoids network predicting f_x and f_y in pixel unit directly, whose values are often large and pose numerical difficulties in optimisation.

In practice, we found that optimising the square root of s_x and s_y, denoted by $\tilde{s}_x$ and $\tilde{s}_y$ respectively, leads to slightly better results, *i.e.*

$$f_x = \tilde{s}_x^2 W \tag{13}$$
$$f_y = \tilde{s}_y^2 H, \tag{14}$$

where $\tilde{s}_x$ and $\tilde{s}_y$ are initialised to 1.0 too. Table 3 shows a quantitative comparison of the novel view rendering quality using these two parameterisations.

Focal Impl.	Fern	Flower	Fortress	Horns	Leaves	Orchids	Room	Trex	Mean
s_x, s_y	21.51	25.31	26.54	22.98	**18.80**	**16.51**	25.17	**22.62**	22.43
$\tilde{s}_x^2, \tilde{s}_y^2$	**21.83**	**25.34**	**26.55**	**23.13**	18.73	16.50	**25.73**	22.49	**22.54**

Table 3. Quantitative comparison (PSNR on novel views) of two different focal length parameterisations on LLFF-NeRF dataset. Higher is better.

Dataset Details

We select two sequences from RealEstate10K [Zhou et al. 2018] and one video from Tanks&Temples dataset[Knapitsch et al. 2017]. The details of the videos and pre-processing procedures are listed in Table 4.

Dataset	Video ID/name	Original fps	Original res.	Training fps	Training res.
RealEstate10K	MVVJodQ50HQ	30	1920x1080	5	1920x1080
RealEstate10K	OT04jHhqYyw	30	1920x1080	5	1920x1080
Tanks&Temple	Advanced/Ballroom	images	1920x1080	N/A	1920x1080
Our data	Globe - rotation	4	6240x4160	4	780x520
Our data	Cauliflower - zoom-in	4	6240x4160	4	780x520

Table 4. Dataset details. We conduct experiments with several video segments from two public dataset RealEstate10K and Tanks&Temples, as well as two video clips captured by ourselves. The video ID entries for RealEstate10K videos denote their YouTube video IDs.